Accurate ab initio determination of ballistic electron emission spectroscopy: Application to Au/Ge

A. Gerbi, C. González, R. Buzio, N. Manca, D. Marrè, L. D. Bell, D. G. Trabada, S. Di Matteo, P. L. de Andres, and F. Flores

Phys. Rev. B **98**, 205416 — Published 21 November 2018

DOI: 10.1103/PhysRevB.98.205416

Accurate *ab initio* determination of Ballistic Electron Emission Spectroscopy: application to Au/Ge

A. Gerbi[1], C. González[2],* R. Buzio[1], N. Manca[1,3], D. Marrè[1,3], L. D. Bell[4], D. G. Trabada[2], S. Di Matteo[5], P. L. de Andres[6], and F. Flores[2]

[1]*CNR-SPIN Institute for Superconductors, Innovative Materials and Devices, Corso Perrone 24, I-16152 Genova, Italy*

[2]*Física Teórica de la Materia Condensada-IFIMAC, U. Autonoma de Madrid, E-28049 Madrid, Spain*

[3]*Dipartimento di Fisica, Universita degli Studi di Genova, via Dodecaneso 33, Genova, Italy*

[4]*Jet Propulsion Laboratory, CALTECH, 4800 Oak Grove Dr. Pasadena, CA 91104, USA*

[5]*Univ. Rennes, CNRS, IPR (Institut de Physique de Rennes) - UMR 6251, F-35000 Rennes, France and*

[6]*Instituto de Ciencia de Materiales de Madrid-CSIC, Cantoblanco, E-28049 Madrid, Spain*

(Dated: October 29, 2018)

Abstract

Ab initio non-equilibrium Keldysh formalism based on an N-order renormalisation technique is used to compute $I(V)$ Ballistic Electron Emission Microscopy characteristics at the Au/Ge(001) interface. Such a formalism quantitatively reproduces precise experimental measurements under ultra-high vacuum and low-temperature conditions. At $T = 0$ K the ballistic current follows the law $(V - V_{SB})^{2.1}$, V_{SB} being the Schottky barrier. At $T > 0$ K, temperature effects become significant near the onset and must be taken into account to identify an accurate value for V_{SB} from a best-fit procedure. We find two values for V_{SB}: 0.67 and 0.75 eV, which we associate with two different atomic registries at the interface.

PACS numbers: 73.23.Ad,73.30+y,73.40.-c,68.37.-d

Keywords: Condensed Matter and Materials Physics. Research Areas: Transport, nano, interfaces. Physical Systems: Au, Ge, metal-semiconductor. Properties: Schottky barrier. Techniques: Ballistic Electron Microscopy.

I. INTRODUCTION

Scanning Tunneling Microscopy (STM) is a technique that has revolutionised the characterisation of nanostructures on surfaces due to its atomic resolution and its ability to manipulate atoms and molecules on a surface.[1] A significant extension of STM is Ballistic Electron Emission Microscopy (BEEM), that was introduced by Bell and Kaiser to study buried objects like the metal-semiconductor interface (MSI).[2] In particular, BEEM is an invaluable tool with potential to characterize with nanometric resolution the all-important technological system formed by the metal-semiconductor interface, as it has been experimentally demonstrated[3,4] and, theoretically rationalized[5]. Indeed, the MSI is the basis for rectifying devices widely found in electronics; the knowledge of their characteristics with nanoscopic resolution is of primary importance as their typical sizes diminish towards the nanoscale. Therefore, it is clear the importance of the determination of V_{SB}, which can only be achieved with precision by a suitable combination of carefully controlled experiments and accurate theoretical simulations.

However, a significant drawback to faithfully extract information from BEEM has been the lack of a comprehensive first-principles theory able to describe with internal consistency the whole tip-metal-semiconductor system in a BEEM setup.[6] Here, we introduce an *ab initio* formalism based on non-equilibrium Keldysh's Greens functions, that consistently includes multiple-scattering and coherence along *all* the steps in the BEEM experiment. Furthermore, since it only involves N-order calculations, it allows the study of large enough three-dimensional atomistic models that can be realistically compared to experiments.[7] Therefore, we combine our own ultra-high vacuum (UHV), low-temperature BEEM experiments for the Au(001)/Ge(001) interface with the *ab initio* theory presented below to extract accurate values for the Schottky barrier.

Good agreement between theory and experiments requires two slightly different values for V_{SB}: 0.67 ± 0.01 and 0.75 ± 0.01 eV. We attribute such a double barrier to the existence of different atomic registries at the interface (details are given in the Appendix A). Our calculations for alignment of levels across the interface for two Density Functional Theory (DFT) optimized models predict a difference in their respective V_{SB} of 0.10 ± 0.01 eV, which is comparable to the one obtained from our best-fit to experiments. The proposed procedure yields a remarkable accuracy in the determination of V_{SB} ($\approx \pm k_B T$ eV) due to the *ab initio*

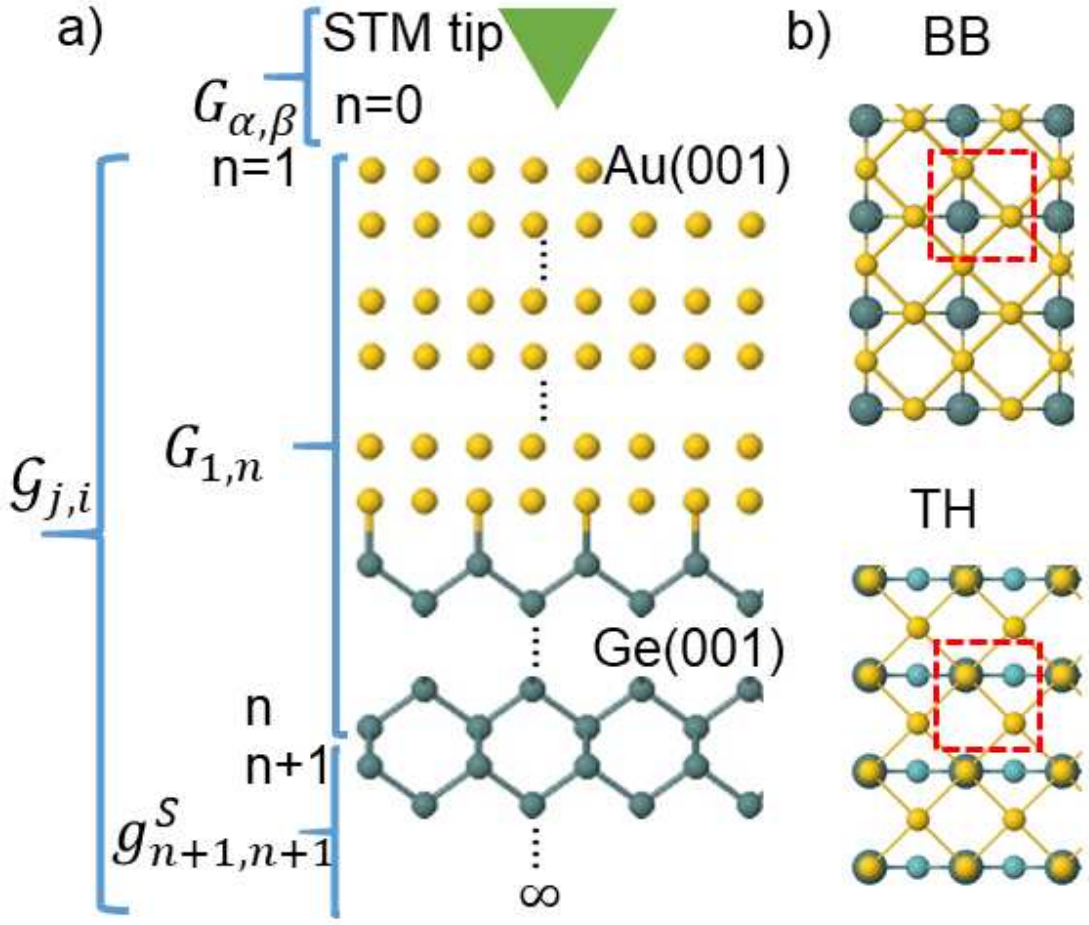

FIG. 1. (color online) (a) Schematic BEEM setup: carriers are injected from a STM tip (green, layer $n = 0$) into a metal slab (yellow, from superlayer 1 to superlayer m) adsorbed on a thin semiconductor slab representing the interface region (blue, from superlayer $m+1$ to n, $p = n - m$ superlayers) that is connected to the semi-infinite semiconductor acting as collector (blue, from superlayer $n + 1$ to ∞). Green's functions $G_{l,m}$ are computed adding one superlayer at a time recursively, while $g^{(S)}_{n+1,n+1}$ are computed via a decimation technique (cf. Appendix B). (b) Two $\sqrt{2} \times \sqrt{2}$R 45° optimized interfaces ($\epsilon = 0.016$). BB: Au on both bridges of Ge(100). TH: Au on atop and hollow sites.

determination of the power-law used to find a best-fit to experiments, and to the inclusion of temperature effects via the Fermi-Dirac distribution above and below the Schottky barrier.

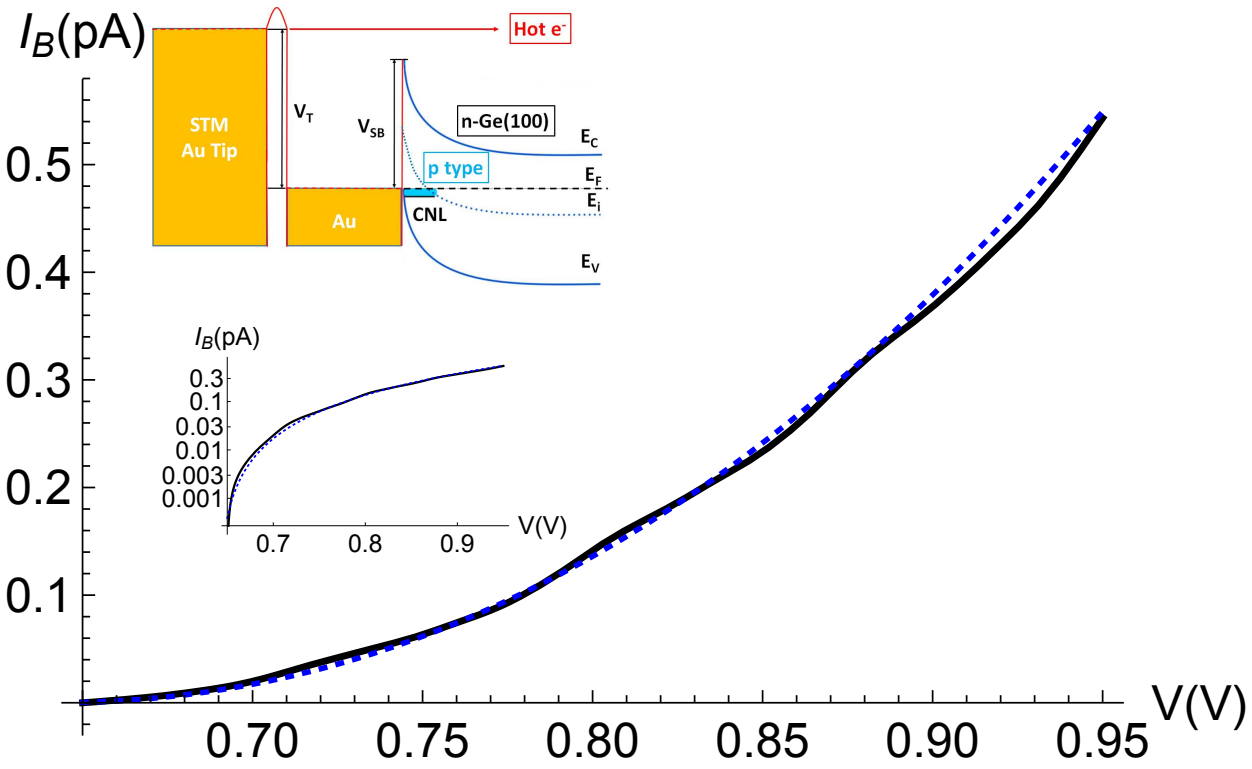

FIG. 2. (color online) BEEM $I_B(V)$ characteristics from *ab initio* calculations computed from Eq. (1) on the 9th superlayer of Ge(100). We have considered the BB configuration, with a tip-sample distance of 5 Å, $V_{SB} = 0.649$ V, $\eta = 0.005$ V, and 9216 k-points in the IBZ. The dotted blue line is the best-fit using Eq. (2) with $\mu = 2.1$ and $\alpha = 6.5$ pA $\mathrm{V}^{-\mu}$. Lower inset shows the same plot in log scale. Upper inset: bands alignment between tip-metal-semiconductor (notice the strong inversion).

II. EXPERIMENTAL: AU/GE

Because its higher electron and hole mobility relative to silicon, Ge has received considerable attention for high-speed metal-oxide-semiconductor devices (e.g. MOSFETs).[8–12] However, a notable disadvantage that has so far limited performance in Ge MOSFET n-channel devices is the strong Fermi Level Pinning at the charge neutrality level (CNL),[13–15] creating a high Schottky barrier and preventing the formation of low resistance contacts.[9,16] Curiously enough, no BEEM data have been reported so far in literature for the metal/Ge interface, although some works have been published on buried Ge dots, and $Si_{1-x}Ge_x$ strained interfaces[17,18].

In our experiments, a Ge(100) wafer (n-type, Sb-doped, 3.97-4.46 Ωcm, MTI Corporation) was cut into pieces and cleaned to remove the native oxide and to obtain a hydrogen-terminated Ge(100) surface.[12] The cleaned Ge pieces were loaded within few minutes into the UHV deposition chamber for the Au contact fabrication, obtained by thermal evaporation through a shadow mask (nominal thickness and area of the metal contact are ≈ 20 nm and 2.1 mm^2, respectively). The Ohmic back contact was fabricated by depositing a thick Al film by pulsed laser deposition from a high purity target.[19] Interpolation of room-temperature current-voltage characteristics using conventional thermionic emission theory provided an effective Schottky barrier height $V_{SB} = 0.62$ eV and an ideality factor $n = 1.04$, in line with previous reports.[20]

BEEM measurements have been performed under UHV with a base pressure of 3×10^{-10} mbar using a modified commercial STM equipped with an additional low-noise variable-gain current amplifier.[21–23] To improve the signal-to-noise ratio, data was taken under dark, with tunneling current I_T in the range 0.5 to 5 nA, and at $T = 80$ K. For the acquisition of each BEEM spectrum, the tip voltage V was ramped under feedback control, keeping the tunneling current I_T constant. A typical spectrum consisted of 100-3600 averaged curves, and each one was acquired in ≈ 1 min to 10 s. Individual BEEM spectra were acquired from a grid on an area of lateral size at least 400×400 nm^2, with spacing between two neighbor spectra of at least 10 nm (to reduce local damage induced by the electron beam). For a typical Au thickness of about 10 nm and propagation perpendicular to a $\{001\}$ plane we estimate that the BEEM electronic spot covers an area of about 10×10 nm^2 at the interface; such a region is not uniformly illuminated, it displays lines with a typical width of ≈ 1 nm due to diffraction-like elastic scattering from electronic bands, e.g. see Fig. 3 in[24] or Fig. 9 in[6]. Although the lines are clearly thin enough to yield nanometric resolution at the interface while scanning a step, a grain boundary or even a point defect, the existence of symmetry related lines separated by about 10 nm add contributions from SBHs of regions apart by the same distance. Therefore even a single I(V) curve should show the signature of both domains for an interface made of two domains separated by ≈ 10 nm with different SBHs. Such multi-contribution from several domains is reinforced when I(V)s taken in points on the metal surface separated by more than 10 nm are averaged together to increase the signal-to-noise ratio, as it has been made in this work. Noise current fluctuations in individual raw spectra amounted to ≈ 12 fA rms. Such a low noise level enables an accurate comparison

between theory and experiment. The many different spectra acquired on different locations of the gold electrode indicated a high spatial homogeneity for the Schottky barrier height distribution (i.e., good reproducibility). Typical spectra showed a threshold around 0.66 eV. However, interpolation with simplified BEEM models for a single Schottky barrier was not satisfying in some respects (see below). In what follows, we consider the BEEM-current for electrons only, because Ge is n-doped and has an inversion layer (the Fermi level is very close to the valence band edge), making the transport by holes difficult to analyze without including the long semiconductor depletion region in the theory.

III. THEORY

To obtain an *accurate* value for V_{SB} it is necessary to resort to first-principles theory to get the best possible fit to experimental data, avoiding unnecessary and unwarranted assumptions. Previous theoretical approaches have addressed the BEEM current as a sequence of steps for (i) tunnelling, (ii) propagation through the metal base, (iii) transmission at the metal-semiconductor interface, and (iv) propagation in the semiconductor collector.[5,25] Each of the steps has been treated to different sophistication levels, sometimes mixing quantum-mechanics in some places with semi-classical approaches in others.

Here we introduce a coherent approach based in Eq. (1) (below) that improves over previous calculations by joining all processes in a single *self-consistent* step, therefore increasing our ability to determine an accurate theoretical I(V) characteristics that could be compared with experimental data to extract the much sought value of V_{SB}. Indeed, an approach breaking down separately the processes contributing to BEEM could not determine the Schottky barrier with better accuracy than the model (i) used to describe the transmission through the interface and (ii) the currents coming in and out from that region. In particular, to reproduce our experimental data we build a 3D atomistic model consisting of a Au(100) slab made of 50 superlayers (cf. Appendix B for an explanation of the term *superlayer*) consisting of bilayers of Au(001) planes with AB stacking and $\sqrt{2} \times \sqrt{2}$ R 45° 2D unit cell (i.e. 200 atoms in the slab unit cell) in close contact to 4 superlayers made of Ge(100) planes with ABCD stacking sequence and 1×1 2D unit cell (i.e. 16 atoms in the slab unit cell). That region, which includes the metal-semiconductor interface, is grown on a semi-infinite Ge(100) surface (collector), which is computed using the same scheme but keeping bulk-like

values for the interaction between layers. Therefore, we incorporate a detailed *ab initio* description of the atomic positions and the charge redistribution at the interface region, and the currents in that region are computed by bundling everything together in Eq. (1). Such a specific description of the system allows us to validate a particular power-law for the given interface under consideration. Figure 1-(a) shows a scheme for our BEEM model and details of the different Green's functions involved in the calculation are given in Appendix A.

For electrons propagating with energies between E and $E + dE$ at $T = 0$K (assuming no exchange of energy with the medium), the ballistic current injected from the STM tip into the $n + 1$ superlayer (i.e., p semiconductor superlayers below the MSI; a place where the system can be safely matched to the semi-infinite semiconductor acting as collector) is given by,[7]

$$\frac{\partial I}{\partial E} = \frac{4e}{\hbar} \int_{\mathrm{IBZ}} d^2\vec{k}_{\parallel} \sum_{(l,l')<n+1} \mathrm{Tr}\left[\mathcal{D}^R_{l,1}\ \Gamma_{1,1}\ \mathcal{D}^A_{1,l'}\ \Gamma_{l',l}\right] \tag{1}$$

$$\mathcal{D}^R_{l,1} = \left(\delta_{l,l''} - G^R_{l,l'''} t^S_{l''',l'''+1} g^{R\ (S)}_{l'''+1,l'+1} t^S_{l'+1,l''}\right)^{-1} G^R_{l'',1}$$

$$\mathcal{D}^A_{1,l} = G^A_{1,m''} \left(\delta_{m'',l} - t^S_{m'',m'+1} g^{A\ (S)}_{m'+1,l'+1} t^S_{l'+1,l'} G^A_{l',l}\right)^{-1}$$

$G^{R,A}_{l,l'}$ are Green's functions taking care of propagation and multiple-scattering through the m superlayers of the metal base plus p superlayers of the semiconductor. These functions are computed adding one superlayer at a time using an N-order recursive technique based on Dyson's equation as explained in Appendix B. $g^{R,A(S)}_{m+1,m'+1}$ are retarded and advanced Green's functions of the semiconductor computed using a decimation technique (cf. Fig 1).[26] On the other hand,

$$\Gamma_{l',l} = t_{l',n+1} \rho^{(S)}_{n+1,n+1} t_{n+1,l}$$

$$\Gamma_{1,1} = t_{1,0} \rho^{(T)}_{0,0} t_{0,1}$$

are injection rate matrices from the metal to the semi-infinite semiconductor region (S), and from the tip (T) to the metal. We notice that injection of tunneling electrons can be treated using similar techniques. Therefore, we take advantage of introducing the Green's functions G that describe accurately the metal base and a few semiconductor superlayers ($p = 4$) that correspond to the geometrical configuration we have independently determined using ab-initio plane-waves DFT (cf. Appendix A). Finally, the resulting Green's functions are

coupled to the semi-infinite semiconductor via the density of states $\rho^{(S)}_{n+1,n+1}$ in Eq. (1) that is calculated using the decimation technique. The sheer advantage of using N-order techniques is that the computational effort scales linearly with the size of the system, allowing us to set up models with a realistic enough size so they can be safely compared with experiments (i.e., including hundreds of layers or more).

We notice that even if the ballistic current above is actually a parameter-free expression, it is usual to add an small imaginary part to the energy ($E \rightarrow E + i\eta$) to: (1) smooth out peaks, substituting the $k_{\|}$ integration over the 2D interface Brillouine zone (IBZ) by a summation on a set of special k-points, and (2) ensure convergence of outgoing waves.

These calculations have been programmed so they can use as input either *ab initio* bulk bands described by tight-binding parameters,[27] or electronic structure bands calculated with a local combination atomic orbitals (LCAO) DFT-code.[28] We have checked both and we have found only minute differences when the agreement between both approaches is good. The former approach is probably simpler to use, while the latter would be necessary when dealing with materials not listed in the literature or if a complete description of the atomic configuration and charge distributions is required. For our case of study all the results in this work have been obtained relying on Ge-bands in[27] while the Au-bands as well as the interface are parametrized using the LCAO-DFT data.

Since the tip-metal distance in a BEEM experiment is large and the tip geometry is sharp, the use of a single apex with an s-orbital ($\rho^{T}_{0,0}$) is justified. On the other hand, several atoms on the periodic surface can contribute to the injection, possibly bringing about coherence effects which are fully accounted for by this formalism. In fact, because $k_{\|}$ is conserved at the ideal MSI, the initial energy and momentum distribution at the surface influences the BEEM current and permits to study with submolecular resolution organic molecules deposited at the surface.[29,30] Finally, we remark the instrumental advantage of dealing with an N-order method to calculate the Green's functions, which becomes crucial to obtain the BEEM current on a realistic MSI.[31]

The atomic configuration at the experimental interface is not currently available from structural techniques. Therefore, we have optimized plausible models using DFT.[32] We construct candidate interfaces from 1×1 surfaces: to compensate for Ge and Au 2D different lattice constants, we rotate one against other by 45° to minimize interfacial strain. The resulting $\sqrt{2} \times \sqrt{2}$ R 45° Au(100)/Ge(100) displays a $\epsilon = 1.9\%$ mismatch between both

lattices across the interface; the remaining stress can be reasonably accommodated by defects, in particular by different stackings. DFT optimization yields two competing local minima with an enthalpy difference of less than 0.1 eV per atom in the interface, supporting the appearance of both patches in the microscopic interface in the experiment. In the first configuration (frontal view in the upper part of Fig. 1-(b), both Au atoms in the 2D unit cell are located over the two bridges (named BB, the preferred one). In the second one (labelled TH), one Au atom is located atop, while the other is on hollow, cf. the lower part in Fig. 1-(b). The red squares indicate the size of the unit cell in the DFT simulation. These geometries have been fully relaxed to analyze the electronic structure of the MSI (details in Appendix A).

Fig. 2 shows the result of using Eq. (1) to compute the ballistic current for the BB Au(001)/Ge(001) interface (black continuous line). Such a plot immediately suggests that the available phase space, $\frac{\partial I}{\partial E} \propto (E - V_{SB})^{\mu-1}$, plays a significant role (μ takes a value that only depends on details of the system like the band structure of the semiconductor or the atomic arrangements at the interface). Therefore, the ballistic current in a small interval of energies around V_{SB} can be easily obtained from the differential conductance (blue dashed curve in Fig. 2):

$$I_B(V - V_{SB}) \propto \int_{V_{SB}}^{V} (E - V_{SB})^{\mu-1} dE \ \propto (V - V_{SB})^{\mu} \ ; \ V_{SB} \leq V \tag{2}$$

Such a free-electron model has been proposed in the literature with $\mu = 2.0$,[2] or $\mu = 2.5$,[33] depending on different hypothesis on the transmission coefficient at the MSI, cf. Appendix C. It allows a most simple procedure to get a value for V_{SB} by a best-fit to experimental data, with an error bar of $\approx \pm 0.05$ eV which is mainly originated in the different values available for μ.[34] Therefore, to improve the accuracy on the determination for V_{SB} it is desirable to know a better value for μ corresponding to a given metal-semiconductor combination; we obtain its specific value for Au(001)/Ge(001) by comparing our *ab initio* Eq. (1) to the simplified model of Eq. (2). We find (Fig. 2) that $\mu = 2.1 \pm 0.1$ yields a best-fit (the incertitude is associated to different tip-sample distances). It is interesting to notice that this implies for our particular Au/Ge system a quantum-mechanical transmission at the interface quite constant, with an smoother energy dependence than the square root associated with a square barrier, cf. Appendix C.

To determine V_{SB} with an accuracy of $\approx \pm 0.01$ eV it is also necessary to care at least about two non-ballistic contributions: inelastic losses and thermal effects. By limiting the energy interval to $\mid V' = V - V_{SB} \mid < 0.2$ eV around the onset secondary electrons are mostly removed since their probability to be reinjected is low. Therefore, they can be accounted for by an approximately constant factor describing attenuation, $\sigma = e^{-\frac{l}{\lambda}}$, where l represents a typical length of the system and λ is the mean free path related to the optical potential due to inelastic interactions, $\lambda(E) = \frac{\hbar v(E)}{2\eta(E)}$.[35–38] We notice that the energy dependence of the optical potential is considerably smoothed if $\mid V' \mid < 0.2$ eV, which allows us to take a constant value for η. Under these conditions, the limiting value $\eta = 0$ is simply recovered by multiplying the current in Eq. (1) by the inverse of σ. Since we use in the IBZ around 10000 special points to cover a band of approximately 1 eV, a typical value for η would be $\frac{1}{100}$ eV. In practice, we use $\eta = 0.005$ eV, that corresponds to an attenuation length of $\lambda \approx 1500$ Å and is much larger than the metallic base ($l \approx 200$ Å), which is another reason to use a constant value within $\Delta V < 0.2$ eV from the onset. Finally, $\eta = 0.005$ eV ensures both good convergence with our choice for special points and describes well the damping of the ballistic current in this small energy range.

Thermal effects, on the other hand, are most easily incorporated by taking into account the Fermi-Dirac distribution, $f(E,T)$. Then, Eq. (2) can be re-written:

$$I_B(V - V_{SB}, T) = \alpha \int_0^\infty (E - V_{SB})^{\mu-1} [f(E - V) - f(E)] \, dE = \tag{3}$$

$$= -\alpha \, (k_B T)^\mu \, \Gamma[\mu] \, \mathrm{Li}_\mu \left(-e^{\frac{V - V_{SB}}{k_B T}} \right) \tag{4}$$

where $\alpha = I_{EXP}(0,T)$ is a free parameter to adjust the absolute value of the model to the experiment at a single energy value ($V = V_{SB}$ has been used here), Γ is the Legendre's Gamma function, and $\mathrm{Li}_\mu(z)$ is the polylogarithm function.[39] While this function is amenable enough to be used around $V' = V - V_{SB} = 0$ to obtain best-fits like the ones given in Fig. 3, an even simpler expression based on a power expansion is provided in Appendix C. We remark that thermal effects cannot be neglected for $\mid V' \mid \lessapprox 2k_B T$, a region significant for the sake of a better determination of V_{SB}. In addition, it is interesting to notice the exponentially decaying contribution of electrons excited by thermal effects over the Schottky barrier in the sub-threshold region ($V' < 0$).[40] Naturally, this contribution can only be used

above the background noise level, which in our experiments appears as a fluctuating value around $10^{-6} < \frac{I_B}{I_T} < 10^{-7}$.

IV. RESULTS AND DISCUSSION

A *simple procedure* to get a value for the Schottky barrier would be to locate the separation between the two regimes in Eq. (C2) of Appendix C, e.g. as signaled by a change from a constant value in the derivative of $\frac{d \log I}{dV}$ (sub-threshold exponential law) to a decreasing value (above-threshold power law). In the inset of the lower panel of Fig. 3 we plot that value for the experimental data (black line) to be compared with the theoretical result from Eq. (3) –red line–. We conclude that the sub-threshold regime in our experiments displays a noise level that makes difficult to identify the onset from the break between both regimes. Therefore, we concentrate on extracting the Schottky barrier by utilizing mostly the above-threshold region (Eq. (C2) of Appendix C). In the upper panel of Fig. 3 we show a fit to experimental values (magenta stars) using Eq. (3) with $\mu = 2.1$ (black lines). The slope of $I(V')$ near $V' \approx 0$ fixes $T \approx 110$ K. The significance of these thermal effects can be seen by comparing with the value $T = 0$ K (blue line). Our determination of the effective temperature predicts a slightly larger value than the nominal experimental one; for comparison, the green line shows that $T = 80$ K yields a slightly poorer fit, indicating that we cannot determine the effective temperature operating on the ballistic electron beam with an incertitude better than a few tens of K. However, one expects the ballistic current to induce slightly larger local temperatures within the electron beams due to inelastic effects.

The log-log plot in the lower panel of Fig. 3 makes clear the necessity to include a second onset near $V' \approx 0.07$ eV to explain the experimental data, $I_B^{\rm EXP} = I_B(V - V_{SB_1}, T) + I_B(V - V_{SB_2}, T)$. Therefore, our best fit includes two Schottky barriers located at 0.67 and 0.75 eV, in the relative proportion of 1:5 (dotted and dashed black lines respectively in the upper panel of Fig. 3). The first Schottky barrier helps to fit well the experimental data in the interval $[0, 0.05]$ eV (upper inset in Fig. 3), including the initial slope expected from the thermal contribution. The second Schottky barrier provides an excellent fit to the experimental data beyond that region, up to ≈ 0.2 eV from the onset.

According to our DFT calculations, the reason for the two Schottky barriers can be physically assigned to the presence of two different atomic configurations coexisting at the

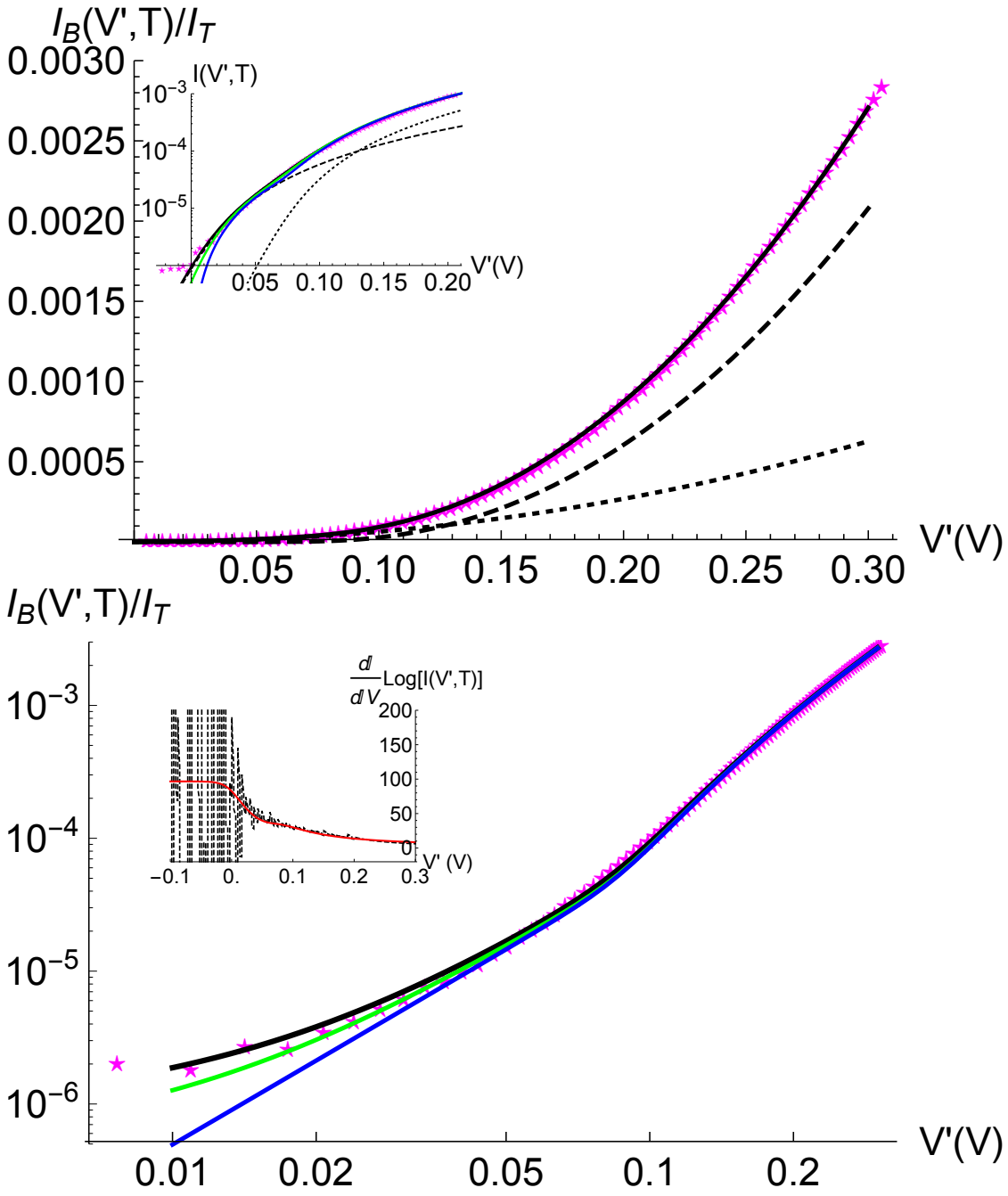

FIG. 3. (color online) Upper panel. Stars (magenta): experimental values. Black continuous line is the best fit to experimental values using Eq. (3) ($\mu = 2.1$), assuming $T = 110$ K and two Schottky barriers at 0.67 and 0.75 V (dotted and dashed black lines respectively). Inset: close-up near the region $V' \approx 0$ V (log plot). Bottom panel. Log-log plot showing the appearance of the second barrier. The green curve is $T = 80$ K, and the blue one is $T = 0$ K. Inset: Derivative of experimental Log(I) (black), compared to the model based in Eq. (3) –red–; notice the exp vs power-law behavior and the fluctuations for $V' < 0$.

interface (BB and TH). Our calculations find a difference between the electrostatic dipole in these two geometries that amounts to ≈ 0.1 eV, which is in good agreement with the value obtained by fitting the experimental data to Eq. (3).[14]

V. CONCLUSIONS

In conclusion, we have developed an N-order parameter-free non-equilibrium Keldysh Green's functions formalism that accurately reproduces the BEEM current normalized to the injected tunnelling intensity. Such a theoretical methodology can be applied to deduce a power-law approximation for the Au(001)/Ge(001) interface, $I_B \propto (V - V_{SB})^{2.1}$, that can be flexibly used to determine an accurate value for the Schottky barrier at the MSI. For $V \approx V_{SB}$ temperature effects become significant, and they should not be ignored. A detailed comparison with experimental data for Au/Ge shows the existence of two different Schottky barriers at 0.67 and 0.75 eV that have been fitted with approximately a ± 0.01 accuracy. These values agree within the estimated error bars with the reported gap of Ge of 0.74 eV at low temperature,[41] and can be associated with the existence of different registries at the interface. The procedure takes into account the effect of secondary electrons on the attenuation of currents due to inelastic e-e interactions. We have chosen to work in the interval $\mid V - V_{SB} \mid < 0.2$ eV because for larger biases, secondary electrons start to play a significant role, and because we can neglect other effects, like electron back-scattering in the semiconductor associated with the electron-phonon interaction.

Acknowledgments. This work has been funded by MAT2017-85089-C2-1-R, MAT2017-88258-R, Maria de Maeztu Programme (MINECO, Spain), MIUR Progetto Premiale 2012 *EOS: organic electronics for advanced research instrumentation* (Italy), and ERC-2013-SYG-610256 (EU).

Appendix A: Atomistic Interface Model

As a method capable of finding reliable geometry configurations we utilize DFT[42,43] and a plane-waves basis to search for viable geometries in the interface of a slab made of 12 layers of Au(001) in contact with a slab made of 16 layers of Ge(001) (CASTEP[32]). The 2D unit cells of Ge(001) and Au(001) are squares with lengths 4.001 and 2.884 Å respectively,

suggesting that a $\sqrt{2} \times \sqrt{2}$R45° configuration for Au would minimize the interfacial stress. Therefore, we explore the two possible high-symmetry models: either the two Au atoms in the surface unit cell take positions over both bridge positions in the Ge surface unit cell(BB), or one is located atop and the other one over the hollow (TH), cf. Fig. 1-(b). Notice that these two models are simply related by a two-dimensional registry shift of $(\frac{1}{2}, 0)$ (fractional coordinates), but imply different relaxations and corrugations of layers. The BB configuration is preferred over the TH one by -0.64 eV, which is small enough to allow the coexistence of patches of both structures. In the BB geometry the closest Au-Ge is 2.75 Å, while in the TH configuration is 2.43 Å. The two Au closest layers to Ge display corrugations of 0.3 and 0.01 Å in the BB configuration; for the TH configuration corrugations are below 0.02 Å for all layers. These calculations have been performed using the CASTEP program with norm-conserving pseudopotentials (*OP.recpot), the Perdew-Burke-Ernzerhof GGA-XC[44], a 610 eV energy cutoff, and a $6 \times 6 \times 1$ Monkhorst-Pack grid[45]. Threshold values for convergence were 10^{-7} eV for the total energy at each self-consistency cycle, 10^{-6} eV for the total energy after each geometry optimization, a maximum force of 0.01 eV/Å, and a maximum displacement of any atom in the optimization cycle of 5×10^{-4} Å.

Once the interface has been accurately relaxed with the plane wave code, we have exported the atomic reconstruction to the LCAO code in order to obtain the tight-binding parameters required by our formalism. We improve the electronic distribution in the first four layers of each material by adding new layers at both sides in the unit cell. The resulting slab is formed by an interface of 42 atoms: 24 Au atoms in 12 layers, and 16 Ge atoms (one per layer) plus two final H atoms saturating the Ge dangling bonds at the end of the slab. We use an spd basis for both Au and Ge that provide a correct band structure in the bulk comparing to the results shown in previous very accurate calculations[27]. The corresponding cutoff radii for Au (Ge) are: $r_c[s] = 4.5$ (5.7) a.u., $r_c[p] = 4.9$ (5.7) a.u. and $r_c[d] = 4.3$ (5.7) a.u. and $r_c[H - s] = 3.8$ a.u. for hydrogen. The first surface Brillouin Zone is sampled with 9216 k-points (the same used in the BEEM simulation), allowing an accurate descritption of the band gap at the bulk.

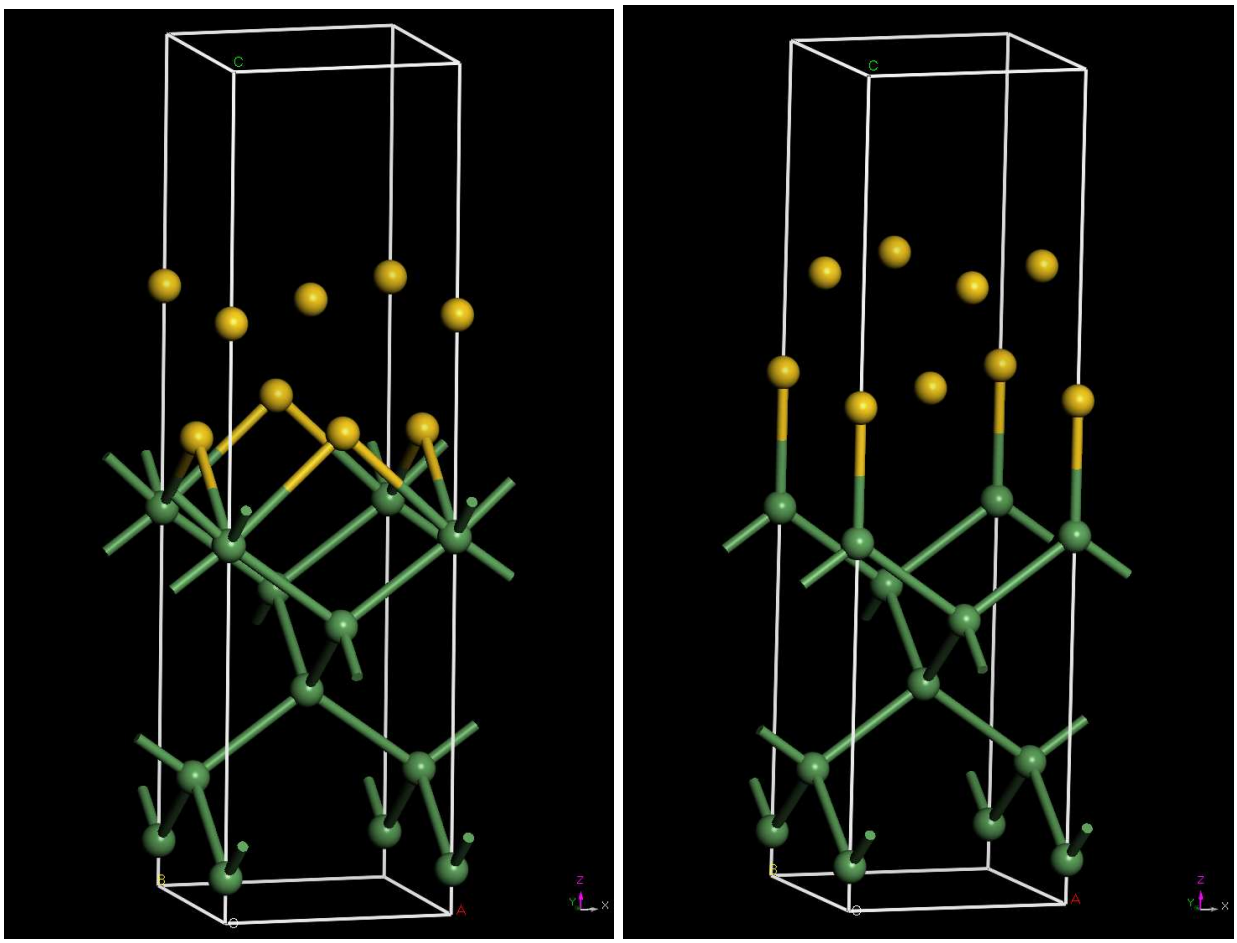

FIG. 4. (color online) 3D view for Ge(001)/$\sqrt{2}\times\sqrt{2}$R45°-Au(001) models. Left panel: Top-Hollow (tH). Right panel: Bridge-Bridge (BB). To increase visibility only two Au-layers and five Ge-layers are shown.

Appendix B: Green's functions transport formalism

The differential current of carriers with energy between E and $E + d\,E$ injected from an STM tip into a semi-infinite semiconductor acting as a collector can be written as:

$$\frac{\partial I}{\partial E} = \frac{4e}{\hbar}\int_{\rm IBZ} d^2\vec{k}_{\|} \sum_{i\leq n, j\geq n+1} {\rm Tr}\left\{ t_{i,j}(\vec{k}_{\|}) \left[\mathcal{G}^{+-}_{j,i}(E,\vec{k}_{\|}) - \mathcal{G}^{+-}_{i,j}(E,\vec{k}_{\|}) \right] \right\} \qquad \text{(B1)}$$

where $\mathcal{G}^{+-}$ are Keldysh's Greens functions[46] and $t_{i,j}$ are hopping matrices describing the interaction between nearby superlayers, with j ($\geq n+1$) located in the semi-infinite semiconductor acting as collector and i ($\leq n$) is located in the region of the metal base plus a few superlayers of semiconductor used to describe the details of the interface, cf. Fig. 1. This

equation reduces to Eq. (1), where two kind of Green's functions are needed: $g^{(S)}_{n+1,n+1}$ to describe propagation through the semiinfinite semiconductor acting as collector, plus $G_{l,m}$ to describe the propagation through the metal base plus a few semiconductor superlayers to better describe the metal-semiconductor interface. The former is obtained from an efficient decimation technique well described in the literature.[26] The latter are computed iteratively solving Dyson's equation as explained in what follows.[7]

The Green's functions, $g_{l,l'}$, for a system composed of l superlayers are obtained from the Green's functions for a system composed of $l-1$ superlayers and the interaction with a single non-interacting superlayer, $t_{l-1,l}$:

$$\begin{cases} g_{l,l'} = \left(\delta_{l,l''} - g^0_{l,l'''} t_{l''',l-1} g^0_{l-1,l'-1} t_{l'-1,l''}\right)^{-1} g^0_{l'',l'} \\ g_{l,1} = g_{l,l'}\ t_{l',l-1}\ g^0_{l-1,1} \end{cases} \tag{B2}$$

This equation is solved iteratively starting from the diagonal resolvent for a single isolated superlayer, $g^0_{l,l} = \left(E - H^0_{l,l}\right)^{-1}$, to construct successively the pairs $(g_{21},\ g_{22})$, (g_{31}, g_{33}), etc, to finally get $(g_{l,1}, g_{l,l}) = (G_{l,1}, G_{l,l})$.

For example, at the starting point a composed superlayer ($l = 2$) is made by joining two single non-interacting superlayers ($l = 1$),

$$\begin{cases} g_{22} = \left(1 - g^0_{22} t_{21} g^0_{11} t_{12}\right)^{-1} g^0_{22} \\ g_{21} = g_{22}\ t_{21}\ g^0_{11} \end{cases} \tag{B3}$$

which can be repeated iteratively to get a composed superlayer with $l = 3$, etc. Such a procedure constitutes an effective N-order recursion method.[47]

Appendix C: Ballistic Model

Eq. (2) can be interpreted in physical terms for ballistic electrons by integrating the flux of carriers perpendicular to the interface,

$$I_B(V) \propto \int v_\perp \left[F(E-V) - F(E)\right] \theta(E - V_{SB}) \mathcal{T}(E, V_{SB}, k_\parallel)\ d^3\vec{k} \propto \tag{C1}$$

$$\propto \int_{V_{SB}}^{V} d\ E \int_0^{\sqrt{2(E-V_{SB})}} k_\parallel \mathcal{T}(E, V_{SB}, k_\parallel) d\ k_\parallel \propto$$

$$\propto \int_{V_{SB}}^{V} (E - V_{SB})^{\mu-1} d\ E \ \ ; \ \ V_{SB} \leq V$$

where μ takes a value that depends on the model for the transmission coefficient, $\mathcal{T}$, e.g.,[2,33]

$$\begin{cases} \text{if } \ \mathcal{T}(E, V_{SB}, k_{\parallel}) \propto 1 \ \ \Rightarrow \ \ \mu = 2, \\ \text{if } \ \mathcal{T}(E, V_{SB}, k_{\parallel}) \propto \sqrt{2(E - V_{SB}) - k_{\parallel}^2} \ \ \Rightarrow \ \ \mu = 2.5 \end{cases}$$

Therefore, Eq. (C1) shows how the available phase space for injection of carriers (including a transmission coefficient) determines the purely ballistic I(V) characteristics near the onset, as written in Eq. (2).

Finally, we notice that Eq. (4) can be expanded around $V' = V - V_{SB} \approx 0$ for $\mu > 2$ to yield an approximate expression including thermal effects that only involve powers of V', the exponential function, and the Gamma (Γ) and Riemann's Zeta (ζ) functions. In the simplest case we have for $V' < 0$,

$$I_B(V', T) \approx \alpha \frac{2^{\mu} - 2}{2^{\mu}}\ \zeta(\mu)\ \int_0^{\infty} \frac{E^{\mu-1}}{e^{-\frac{E-V'}{k_B T}} + 1}\ d\ E \approx \alpha \frac{2^{\mu} - 2}{2^{\mu}}\ \zeta(\mu)\ \int_0^{\infty} E^{\mu-1} e^{-\frac{E-V'}{k_B T}}\ d\ E =$$

$$= \alpha \frac{2^{\mu} - 2}{2^{\mu}}\ \zeta(\mu)\ \Gamma(\mu)(k_B T)^{\mu} e^{\frac{V'}{k_B T}} - ...\ ;\ V' \leq 0 \qquad \text{(C2)}$$

Where the arbitrary constant $\frac{2^{\mu}-2}{2^{\mu}}\ \zeta(\mu)$ has been included so both approximating functions, Eqs. (C2) and (C3), coincide with Eq. (4), e.g. at $V' = 0$ (cf. Fig 5).

On the other hand, for $V' > 0$ we find the following expansion in powers of V':

$$I_B(V', T) \approx \alpha \frac{2^{\mu} - 2}{2^{\mu}}\ \Gamma(\mu)\zeta(\mu)\ (k_B T)^{\mu}\ + \frac{2^{\mu} - 4}{2^{\mu}}\ \Gamma(\mu)\ \zeta(\mu - 1)\ (k_B T)^{\mu-1}\ V' +$$

$$+ \frac{2^{\mu} - 8}{2^{\mu+1}}\ \Gamma(\mu)\ \zeta(\mu - 2)\ (k_B T)^{\mu-2}\ V'^2\ \ ;\ V' \geq 0 \qquad \text{(C3)}$$

Fig. 5 shows a comparison between the exact value from Eq. (4) and the approximations in Eqs. (C2) and (C3) for $V_{SB} = 0.67$ eV and $T = 110$ K. We remark that for $T \neq 0$ K, in the region $V' \approx 0^+$ the BEEM current acquires a quasi-linear dependence on the voltage that cannot be neglected if an accurate determination of V_{SB} is sought.

---

* andrea.gerbi@spin.cnr.it, cesar.gonzalez@uam.es

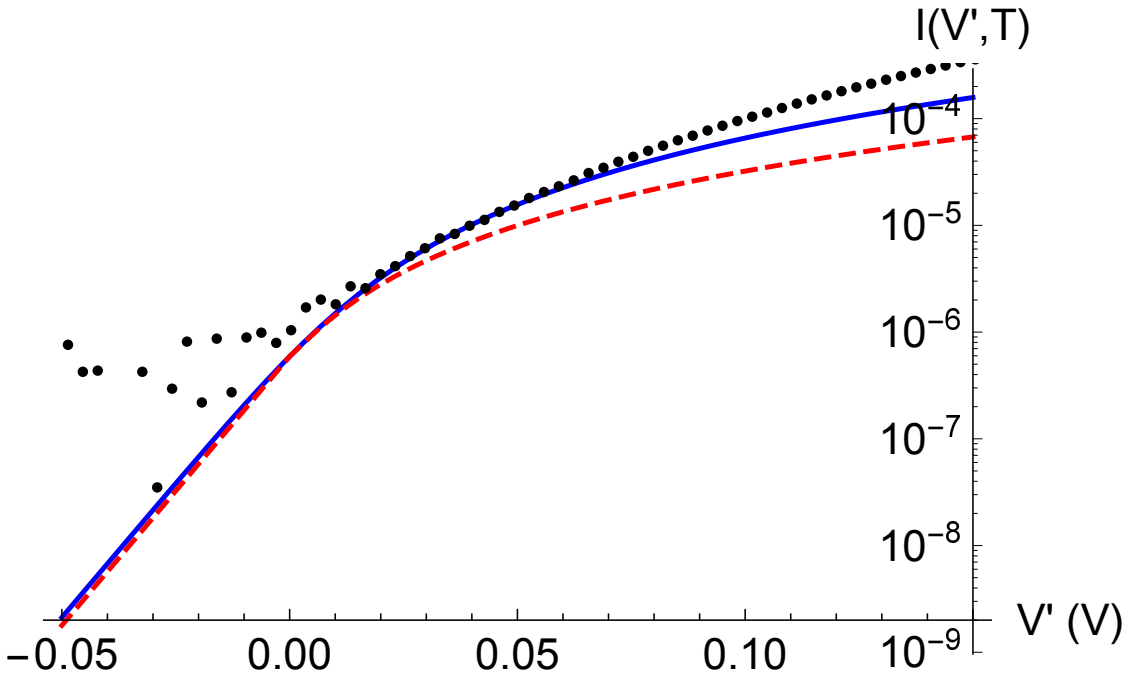

FIG. 5. (color online) Eq. (4) -blue- vs the power-expansion Eq. (C2) -red dashed- for $T = 110$ K. Notice the change from the sub-threshold exponential regime to the above-threshold potential regime. Black dots are experimental values.

[1] G. Binnig and H. Rohrer, Helvetica Physica Acta **55**, 726 (1982).

[2] W. J. Kaiser and L. D. Bell, Phys. Rev. Lett. **60**, 1406 (1988).

[3] A. M. Milliken, S. J. Manion, W. J. Kaiser, L. D. Bell, and M. H. Hecht, Phys. Rev. B **46**, 12826 (1992).

[4] T. Meyer, H. Sirringhaus, and H. von Kaenel, Thin Solid Films **318**, 195 (1998).

[5] F. J. Garcia-Vidal, P. L. de Andres, and F. Flores, Phys. Rev. Lett. **76**, 807 (1996).

[6] P. L. de Andres, F. J. Garcia-Vidal, K. Reuter, and F. Flores, Progress in Surface Science **66**, 3 (2001).

[7] Y. Claveau, S. D. Matteo, P. L. de Andres, and F. Flores, Journal of Physics: Condensed Matter **29**, 115001 (2017).

[8] J. Hu, H.-S. P. Wong, and K. Saraswat, MRS bulletin **36**, 112 (2011).

[9] A. Chroneos, U. Schwingenschloegl, and A. Dimoulas, Annalen der Physik **524**, 123 (2012).

[10] G. Scappucci, G. Capellini, W. M. Klesse, and M. Y. Simmons, Nanoscale. **5**, 2600 (2013).

[11] J. Robertson and R. M. Wallace, Materials Science and Engineering **88**, 1 (2015).

[12] P. Ponath, A. B. Posadas, and A. A. Demkov, Applied Physics Reviews **4**, 021308 (2017).

[13] C. Tejedor, F. Flores, and E. Louis, Journal of Physics C: Solid State Physics **10**, 2163 (1977).

[14] F. Flores and C. Tejedor, Journal of Physics C: Solid State Physics **20**, 145 (1987).

[15] S. Sasaki and T. Nakayama, Japanese journal of applied physics **55** (2016).

[16] P. Tsipas and A. Dimoulas, Applied Physics Letters **94**, 012114 (2009).

[17] H. von Känel, T. Meyer, and M. Klemenc, Journal of Electron Spectroscopy and Related Phenomena **109**, 197 (2000).

[18] L. D. Bell, A. M. Milliken, S. J. Manion, W. J. Kaiser, R. W. Fathauer, and W. T. Pike, Phys. Rev. B **50**, 8082 (1994).

[19] R. Buzio, A. Gerbi, D. Marrè, M. Barra, and A. Cassinese, Organic Electronics **18**, 44 (2015).

[20] T. Nishimura, K. Kita, and A. Toriumi, Applied Physics Letters **91**, 123123 (2007).

[21] A. Gerbi, R. Buzio, S. Kawale, E. Bellingeri, A. Martinelli, C. Bernini, C. Tresca, M. Capone, G. Profeta, and C. Ferdeghini, Journal of Physics: Condensed Matter **29**, 485002 (2017).

[22] R. Buzio, A. Gerbi, D. Marré, M. Barra, and A. Cassinese, Journal of Vacuum Science & Technology B **34**, 041212 (2016).

[23] A. Gerbi, R. Buzio, A. Gadaleta, L. Anghinolfi, M. Caminale, E. Bellingeri, A. S. Siri, and D. Marré, Advanced Materials Interfaces **1**, 1300057 (2016).

[24] P. L. de Andres, F. J. Garcia-Vidal, D. Sestovic, and F. Flores, Physica Scripta **T66**, 277 (1996).

[25] M. D. Stiles and D. R. Hamann, Phys. Rev. Lett. **66**, 3179 (1991).

[26] F. Guinea, C. Tejedor, F. Flores, and E. Louis, Physical Review B **28**, 4397 (1983).

[27] D. A. Papaconstantopoulos, *Handbook of the Band Structure of Elemental Solids* (Plenum, 1986).

[28] J. Lewis, P. Jelinek, J. Ortega, A. A. Demkov, D. G. Trabada, B. Haycock, H. Wang, G. Adams, J. K. Tomfohr, E. Abad, H. Wang, and D. A. Drabold, Physical Status Solidi B **248**, 1989 (2011).

[29] A. Bannani, C. Bobisch, and R. Möller, Science **315**, 1824 (2007).

[30] C. A. Bobisch and R. Möller, Chimia **66**, 23 (2012).

[31] The theoretical model has been implemented in a new FORTRAN code that is available under request.

[32] M. D. Segall, P. L. D. Lindan, M. J. Robert, C. J. Pickard, P. J. Hasnip, S. J. Clark, and M. C.

Payne, Z. für Kristallographie **220**, 567 (2005).

[33] M. Prietsch and R. Ludeke, Phys. Rev. Lett. **66**, 2511 (1991).

[34] M. Prietsch, Physics Reports **253**, 163 (1995).

[35] D. Pines, *Elementary Excitations In Solids* (CRC Press, 2018).

[36] J. Pendry, *Low Energy Electron Diffraction* (Academic Press, 1974).

[37] K. Reuter, U. Hohenester, P. L. de Andres, F. J. Garcia-Vidal, F. Flores, K. Heinz, and P. Kocevar, Phys. Rev. B **61**, 4522 (2000).

[38] F. Ladstädter, P. F. de Pablos, U. Hohenester, P. Puschnig, C. Ambrosch-Draxl, P. L. de Andres, F. J. Garcia-Vidal, and F. Flores, Phys. Rev. B **68**, 085107 (2003).

[39] E. W. Weisstein, "Polylogarithm," MathWorld – A Wolfram Web Resource (2018), http://mathworld.wolfram.com/Polylogarithm.html.

[40] H. L. Qin, K. E. J. Goh, M. Bosman, K. L. Pey, and C. Troadec, Journal of Applied Physics **111**, 013701 (2012).

[41] M. Cardona and M. L. W. Thewalt, Rev. Mod. Phys. **77**, 1173 (2005).

[42] P. Hohenberg and W. Kohn, Phys. Rev. **136**, B864 (1964).

[43] W. Kohn and L. J. Sham, Phys. Rev. **140**, A1133 (1965).

[44] J. P. Perdew, K. Burke, and M. Ernzerhof, Phys. Rev. Lett. **77**, 3865 (1996).

[45] H. J. Monkhorst and J. D. Pack, Phys. Rev. B **13**, 5188 (1976).

[46] L. V. Keldysh, Sov. Phys. JETP **20**, 1018 (1965).

[47] B. Biel, F. Garcia-Vidal, A. Rubio, and F. Flores, J. of Phys.: Cond. Matt. **20**, 294214 (2008).